J Mater Sci (2009) 44:4443–4454
DOI 10.1007/s10853-009-3672-8

Microstructure and strengthening mechanisms of a cast Mg–1.48Gd–1.13Y–0.16Zr (at.%) alloy

L. Gao · R. S. Chen · E. H. Han

Received: 19 April 2009 / Accepted: 6 June 2009 / Published online: 23 June 2009

Abstract The microstructure and mechanical properties of a Mg–1.48Gd–1.13Y–0.16Zr (at.%) alloy in the as-cast, solution-treated, peak-aged and over-aged conditions have been investigated by a combination of thermodynamic calculations and experimental approaches. It is shown that both the $Mg_{24}(Gd,Y)_5$ and cuboid-shaped $Mg_5(Gd,Y)$ phases exist in the as-cast sample, which is in good agreement with the Scheil solidification model. The former is dissolved during solution treatment, while the latter persists and coarsens. Subsequent artificial ageing results in the formation of metastable β' precipitates within the α-Mg matrix and along the grain boundaries. The peak-aged alloy exhibits maximum ultimate tensile strength and tensile yield strength of 370 and 277 MPa, respectively, at room temperature. Moreover, the strengths decrease gently from room temperature to 250 °C with a gradual increase of elongation. The strengthening contributions to the yield strength are quantitatively evaluated from individual strengthening mechanisms by using measured microstructural parameters. The modelled yield strengths are compared with the experimental results and a reasonable agreement is reached.

L. Gao · R. S. Chen (✉) · E. H. Han
State Key Laboratory for Corrosion and Protection, Institute of Metal Research, Chinese Academy of Sciences, 62 Wencui Road, Shenyang 110016, People's Republic of China
e-mail: rongshichen@yahoo.com; rschen@imr.ac.cn

L. Gao
Graduate School of the Chinese Academy of Sciences, Beijing, China

Introduction

The combination of low weight, good strength and castability makes Mg alloys promising engineering materials for the automotive and aviation industries [1–3]. Among them, magnesium alloys containing rare earth elements (RE) have received considerable interest in recent years due to their potential for achieving higher strength and better creep resistance at elevated temperatures. The notable examples include experimental and commercial alloys based on the Mg–Gd, Mg–Gd–Y, Mg–Gd–Nd, Mg–Gd–Zn and Mg-Y-Nd systems [4–13]. It was reported that Mg–Gd–Y system alloys, such as Mg–10Gd–3Y–0.4Zr (wt%) [10] and Mg–12Gd–3Y–0.5Zr (wt%) [14], exhibited higher specific strength at both room and elevated temperatures and good creep resistance than conventional Al and Mg alloys, including WE54, whose high temperature strength was the top of existing commercial magnesium alloys [4, 5]. Most of these alloys are precipitation hardenable, and the precipitation of metastable phases contributes mainly to the strengthening of these alloys. In the Mg–Gd–Y alloys, precipitation starts with the formation of β'' phase with a $D0_{19}$ structure and the key strengthening precipitate phases are β' and β_1 [5, 8, 15]. The β' phase has a C base-centred orthorhombic (cbco) structure ($a = 0.64$ nm, $b = 2.22$ nm, $c = 0.52$ nm) [11], and the β_1 phase has a face-centred cubic (fcc) structure ($a = 0.74$ nm). During prolonged ageing, the β_1 phase transforms in situ into the equilibrium phase β, which has a structure isomorphous to Mg_5Gd ($a = 2.23$ nm) [6]. The structure and morphology of these precipitate phases and the precipitation sequence in the alloys have been well established. It is known that the β' phase is the most effective for the strengthening of Mg matrix [11]. However, a systematic description of the strengthening

mechanisms in these alloys is very limited, experimentally and theoretically [5, 7].

The correlation between mechanical properties and microstructures in these alloys is very complex due to the complexity of microstructures. Strengthening is generally factorized according to the strengthening mechanisms: (i) grain boundary strengthening, (ii) solid solution strengthening by alloying elements and (iii) precipitate strengthening. Quantification of individual contributions requires information on the amount of solute, grain size and the features of precipitates (morphology, size and fraction) as a function of thermal history for each alloy composition. Hutchinson et al. [16] modelled these strengthening mechanisms in the commercial alloy AZ91 (Mg–9Al–1Zn (wt%)) and successfully rationalized the evolution of the room temperature hardness. However, similar work on Mg–Gd–Y system alloys is still unsatisfied. Yang et al. [7] investigated quantitatively the individual strengthening contributions in an Mg–9Gd–3Y–0.6Zn–0.5Zr (wt%) alloy. It was found that the yield strength should theoretically reach 740–770 MPa when the alloy was strengthened fully with the precipitation of β'' and β', which is considerably larger than the experimental value. This disagreement was attributed in part to the error of the required microstructural parameters that cannot be easily obtained through experimental approaches. Besides the experimental approaches, thermodynamic calculation is a powerful tool for the quantification, whose current capability allows accurate prediction of the amount of solute, the mole fractions and compositions of all the phases present in a complex multicomponent alloy [17]. Moreover, thermodynamic calculations provide an alternative to costly experimentation as a first step of searching for most effective alloy composition, as well as for choosing procedures of heat treatment, for the expected high strength. While the thermodynamic assessment of Mg–Gd–Y system has been reported [18], calculations on practical alloys were scarce.

In this research, thermodynamic calculations and experimental investigations were performed for the quantification of yield strength. The microstructure and mechanical properties of a Mg–1.48Gd–1.13Y–0.16Zr (at.%) alloy at different steps of processing were examined. Thermodynamic calculations were performed to predict solidification and phase equilibria. The individual strengthening mechanisms were quantitatively related to the microstructures and phase constituents.

Experimental procedures

The alloy was prepared from high purity Mg (>99.95%), Gd (>99%), Y (>99%) and a Mg–30Zr (wt%) master alloy by melting in an electric resistance furnace at about 780 °C under protection with an anti-oxidizing flux. The melt was poured into a mild steel mould preheated to 200–300 °C. The actual chemical composition of the alloy was determined to be Mg–1.48Gd–1.13Y–0.16Zr (at.%) or Mg–8.57Gd–3.72Y–0.54Zr (wt%) by using inductively coupled plasma atomic emission spectroscopy (ICP). In this paper, the atomic percentage is used for all the alloy compositions unless specified otherwise. Specimens cut from the cast ingot were solution treated at 525 °C for 6 h, quenched into hot water at ~70 °C and then subsequently aged at 225 °C for various periods of time.

Vickers hardness testing was performed using 500 g load and a holding time of 15 s. Not fewer than 10 measurements were taken in each alloy. The samples for tensile tests had a gauge length of 5 mm, width of 3 mm and thickness of 2 mm. Tensile tests were performed at an initial stain rate of 1.0×10^{-3} s^{-1} and at temperatures between room temperature and 300 °C. For tests at elevated temperatures, specimens were heated up to the selected temperature within 10 min and were soaked for 5 min before testing. The temperature was controlled within ±2 °C. Three specimens were used for each test condition to ensure the reproducibility of data.

The constituent phases of the alloy in different conditions were identified by X-ray diffraction (XRD) (Rigaku D/max 2400 X-ray diffractometer) with Cu Kα radiation. Microstructures were observed by optical microscope (OM), scanning electron microscope (SEM, Philips XL30 ESEM-FEG/EDAX) and transmission electron microscope (TEM, FEI TECNAL 20) operating at 200 kV. Samples for optical microscopy were etched in a solution of 5 vol.% HNO_3 in ethanol after mechanical polishing to reveal grain boundaries. The mean grain size, d, was measured by the linear intercept method using the equation $d = 1.74\ L$, where L is the linear intercept grain size determined by optical microscopy. No chemical etching was applied to specimens for SEM investigations. Compositions of phases were analysed by energy dispersive X-ray spectrometry (EDS) in the SEM mode. Thin foil specimens for TEM were prepared by punching 3 mm diameter discs, followed by dimple grinding and Ar^+ ion milling in a precision ion polishing system (PIPS, Gatan) operating at 4.5 kV accelerating voltage and ~8° incident angle.

Predictions of microstructure

To determine the microstructure characteristics of the alloy in different states, all the thermodynamic calculations in this work were done with the Pandat software package (CompuTherm, LLC, Madison, WI). In this approach, the Gibbs free energies of individual phases are modelled as a function of composition, temperature, critical magnetic

Table 1 Thermodynamic parameters of the Mg_5Gd and $Mg_{24}Y_5$ phases in the Mg–Gd–Y system [18]

Phase	Sublattice model	Gibbs energy description
Mg_5Gd	Mg_5(Gd, Y)	$G^{Mg_5Gd}_{Mg:Gd} = 5GHSER_{Mg} + GHSER_{Gd} - 60521.6 + 11.2668T$
		$G^{Mg_5Gd}_{Mg:Y} = 5GHSER_{Mg} + GHSER_{Y} - 38549.2 + 7.9020T$
$Mg_{24}Y_5$	Mg_{24}(Gd, Mg, Y)$_4$Y	$G^{Mg_{24}Y_5}_{Mg:Mg:Y} = 28GHSER_{Mg} + GHSER_{Y} - 5932.0$
		$G^{Mg_{24}Y_5}_{Mg:Y:Y} = 24GHSER_{Mg} + 5GHSER_{Y} - 202101.8 + 7.2306T$
		$G^{Mg_{24}Y_5}_{Mg:Gd:Y} = 24GHSER_{Mg} + 4GHSER_{Gd} + GHSER_{Y} - 248763.1 + 19.9258T$
		${}^0L^{Mg_{24}Y_5}_{Mg:Mg,Gd,Y:Y} = -50000.0$

In SI units (Joule, mole of the formula units and Kelvin)

temperature and sometimes pressure and the results are collected in a thermodynamic database. It enables the calculation of multi-component phase diagrams and tracking of individual alloys during heat treatment or solidification by the calculation of phase constituent and its composition [17–19].

Due to the limited reliable concentration range (<1 wt%) for Gd and Y in the commercially available database PanMg for magnesium alloys, the thermodynamic descriptions of the Mg–Gd–Y alloy system developed by Guo et al. [18] were employed for all the calculations in this work. The Gibbs energy functions of element i (i = Mg, Gd, Y), $GHSER_i$, in its standard element reference (SER) state were taken from the SGTE (Scientific Group Thermodata Europe) compilation of Dinsdale [20]. Four phases were included in this study, namely liquid, hcp (Mg), Mg_5Gd and $Mg_{24}Y_5$. The liquid and hcp phases were treated as substitutional solutions, and the intermetallic compounds Mg_5Gd and $Mg_{24}Y_5$ were described using the sublattice model. The thermodynamic parameters describing the Gibbs energies of the Mg_5Gd and $Mg_{24}Y_5$ phases as a function of composition and temperature are given in Table 1. This thermodynamic description has been critically evaluated from the experimental information available in the literatures, although, certainly, this thermodynamic description at the present stage needs further improvement. It should be noted that Zr addition was excluded from the calculation because it had little effect on the phase evolution and only used for grain refinement [19].

Results

Characterization of the alloy in the as-cast state

Typical microstructures of the Mg–1.48Gd–1.13Y–0.16Zr alloy in the as-cast condition are shown in Fig. 1. These reveal that the as-cast alloy consists mainly of the α magnesium phase (a solid solution of Mg containing Gd and Y) as the matrix (arrow 1 in Fig. 1b) and non-equilibrium eutectics (arrows 2 and 3 in Fig. 1b). Some zirconium cores (arrow 4 in Fig. 1a) are observable, which contribute to the grain refinement. With careful TEM investigation, no precipitates can be detected within the α-Mg matrix phase of the as-cast sample. By XRD analysis (Fig. 2), two phases are identified, namely α-Mg and $Mg_{24}(Gd,Y)_5$, where Gd probably substitutes for Y [19]. TEM analysis (inset in Fig. 1b) indicates that arrow 2 corresponds to the $Mg_{24}(Gd,Y)_5$ phase, which is a body-centred cubic (bcc) crystal structure with $a = 1.126$ nm. Isolated cuboid-shaped particles varying in size from 0.5 to 1 μm are frequently observed in association with $Mg_{24}(Gd,Y)_5$, as shown in Fig. 1b (arrow 3). It was identified as the $Mg_5(Gd,Y)$ phase by TEM analysis as shown in Fig. 1c, which is an fcc crystal structure with $a = 2.223$ nm. Figure 1 shows the SEM and TEM micrographs of those phases, and their estimated chemical compositions are given in Table 2. These phases are non-equilibrium ones that form as a result of relatively high solidification rates under practical casting conditions. EDS analysis reveals that under non-equilibrium casting conditions, up to 0.83 at.% Gd and 0.67 at.% Y can be dissolved in the matrix. The volume fraction of the eutectic compounds is about 7 vol.% determined by quantitative metallographic analysis of the as-cast sample.

Figure 3 shows the Pandat simulation of the solidification pathway of the Mg–1.48Gd–1.13Y–0.16Zr alloy, in particular the fraction liquid presents as a function of temperature. Each arrow on the liquid fraction curves of Fig. 3 indicates the appearance of a new phase. It can be seen that the equilibrium solidification calculation indicates no secondary phases form, whereas Scheil calculation (assuming no diffusion in the solid) shows that the $Mg_{24}(Gd,Y)_5$ and $Mg_5(Gd,Y)$ phases should form through the eutectic reactions. This demonstrates that this as-cast alloy followed more closely the Scheil conditions by comparing Fig. 1 with Fig. 3. For the as-cast alloy solidified from superheated melt, the assumption with the Scheil model is generally safe, given the very short solidification time in the permanent mould in

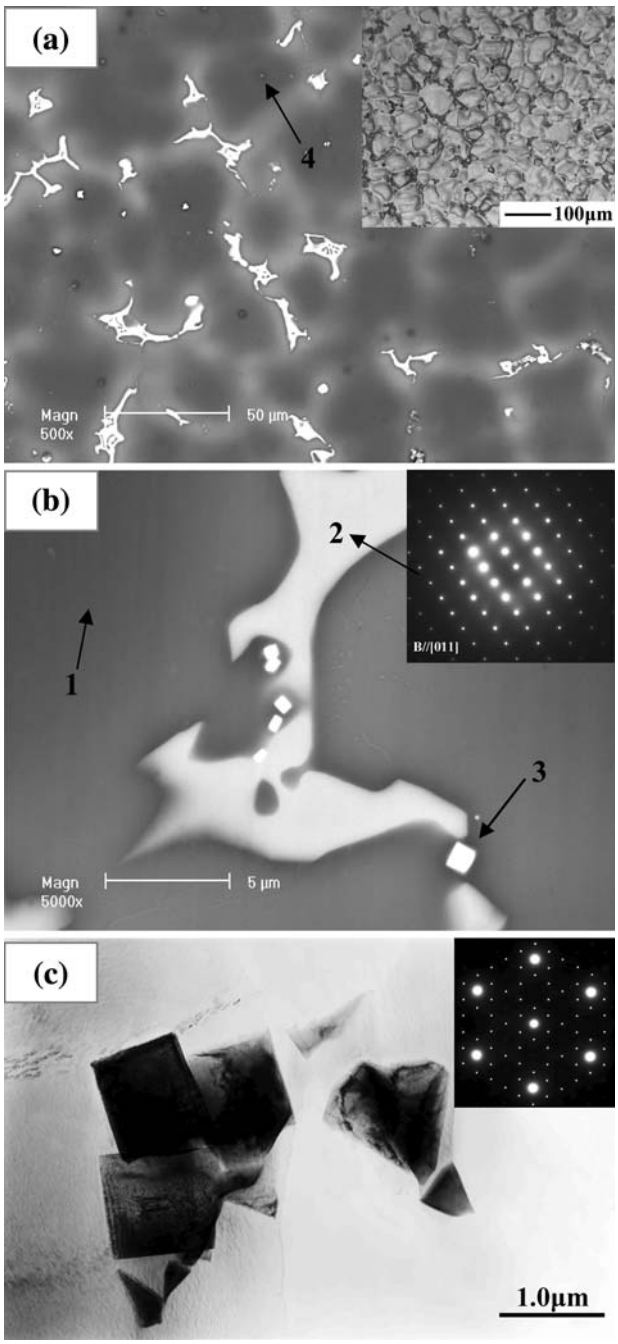

Fig. 1 **a**, **b** SEM images of the as-cast Mg–1.48Gd–1.13Y–0.16Zr alloy and **c** TEM micrograph showing the cuboid-shaped particles together with diffraction pattern of zone axis [111]. Semi-quantitative chemical compositions of the phases marked by the numbers on the images are shown in Table 1

the casting process. The entire calculated solidification pathway, with primary L→α-Mg (arrow 1), secondary L→ α-Mg + $Mg_{24}(Gd,Y)_5$ (arrow 2) and finally Liquid→ α-Mg + $Mg_{24}(Gd,Y)_5$ + $Mg_5(Gd,Y)$ (arrow 3) is in good agreement with the microstructure of this alloy shown in Fig. 1a and b. Therefore, the results confirm the validity of

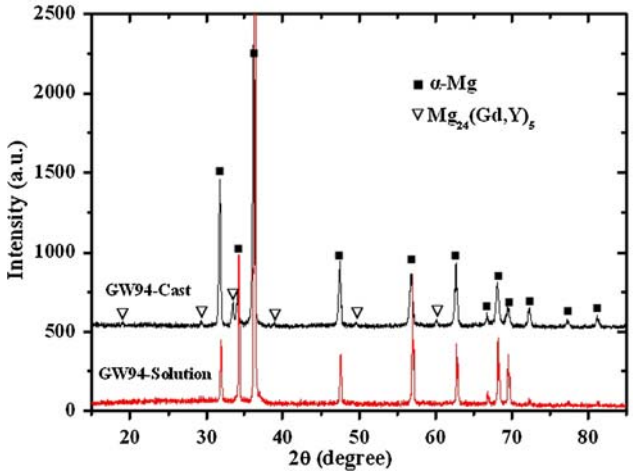

Fig. 2 X-ray diffraction patterns of the Mg–1.48Gd–1.13Y–0.16Zr alloy in the as-cast and solution-treated conditions

the thermodynamic calculations. The corresponding molar fraction of the $Mg_{24}(Gd,Y)_5$ and $Mg_5(Gd,Y)$ phases at the end of Scheil solidification are 4.68 and 1.95 mol.%, respectively. The small amount of the $Mg_5(Gd,Y)$ phase could not be detected by XRD (Fig. 2) but was in fact found and identified by TEM analysis of the alloy in the as-cast state, as shown in Fig. 1c.

Characterization of the solution-treated alloy

Figure 4 shows the optical and SEM microstructures of the Mg–1.48Gd–1.13Y–0.16Zr alloy after the solution treatment at 525 °C for 6 h. The eutectic $Mg_{24}(Gd,Y)_5$ compound has almost completely dissolved into the matrix, resulting in a relatively uniform α magnesium solid solution. XRD pattern (Fig. 2) further confirms the dissolution of the $Mg_{24}(Gd,Y)_5$ phase. This can be understood from the calculated equilibrium phase diagram of the Mg–1.48Gd–*x*Y (at.%) alloy system, as shown in Fig. 5a, where the dashed line indicates the composition investigated. The corresponding phase fraction and concentration in α-Mg at equilibrium as a function of temperature for the Mg–1.48Gd–1.13Y(–0.16Zr) alloy are shown in Fig. 5b and c, respectively. The solubility limits of Gd and Y in Mg are relatively large at the solution treatment temperature of 525 °C (Fig. 5c), where all the second phases should dissolve into the Mg matrix resulting in a single phase microstructure (Fig. 5b). However, about 1 vol.% cuboid-shaped particles (i.e. the black particles in Fig. 4a) are not dissolved but coarsen, as shown in a high-magnification backscattered electron micrograph (Fig. 4b). In addition, the average grain size of the Mg–1.48Gd–1.13Y–0.16Zr alloy is about 61 μm (inset in Fig. 1a) in the as-cast condition and grows up to 108 μm (Fig. 4a) after the solution treatment.

Table 2 Estimated chemical compositions of non-equilibrium structure constituents present in the as-cast Mg–1.48Gd–1.13Y–0.16Zr alloy

Number in Fig. 1	Phase	Fraction (vol.%)	Element [at.%] (wt%)			
			Gd	Y	Zr	Mg
1	Matrix	93	[0.83] (5.06)	[0.67] (2.30)	–	Balance
2	$Mg_{24}(Gd,Y)_5$	6	[7.83] (32.92)	[3.97] (9.46)	–	Balance
3	$Mg_5(Gd,Y)$	1	[23.94] (45.18)	[39.45] (42.34)	–	Balance
4	Zr core	≈0	[0.55] (3.30)	[0.47] (1.61)	[1.04] (3.65)	Balance

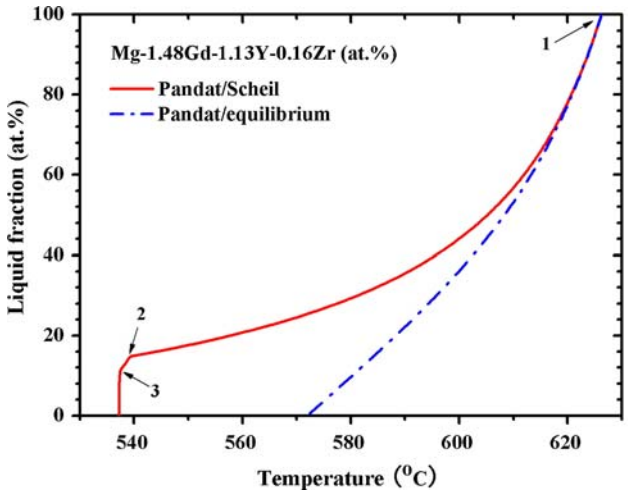

Fig. 3 Simulation of the solidification pathway of the Mg–1.48Gd–1.13Y–0.16Zr alloy by Pandat and the thermodynamic descriptions of Guo et al [18]

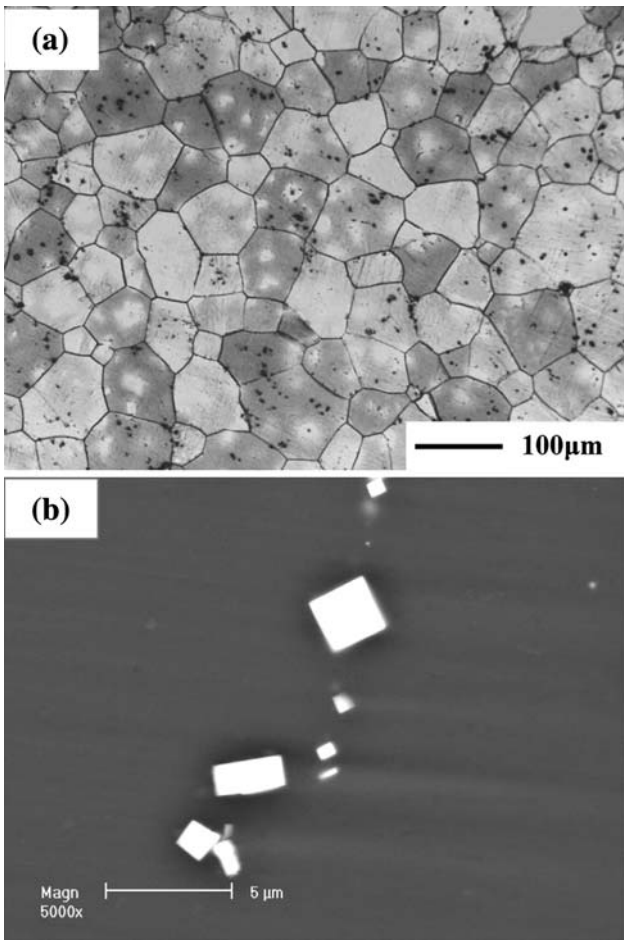

Fig. 4 Microstructures of the Mg–1.48Gd–1.13Y–0.16Zr alloy in the solution-treated condition. **a** Optical image showing the grain size and **b** SEM image showing the cuboid-shaped phase

Age hardening behaviour and peak-aged microstructure

Figure 6 shows a hardness curve of the Mg–1.48Gd–1.13Y–0.16Zr alloy during ageing at 225 °C. Prior to ageing, the initial hardness of the solution-treated alloy is 82 Hv. As can be seen in Fig. 6, the hardness starts to increase rapidly after an incubation period of about 1 h. The peak hardness (129 Hv) attains at about 24 h. Further ageing leads to a rapid decrease in hardness. For microstructural investigation, ageing times of 24 and 168 h were selected which correspond to peak and over-aged conditions, respectively.

The optical microstructure of aged samples is similar to that of solutionized one and the grain size does not change during ageing. Figure 7a and b presents a TEM bright field image and corresponding selected area electron diffraction (SAED) pattern of precipitates in a sample aged at 225 °C for 24 h, with the incident electron beam approximately parallel to $[0001]_\alpha$. It can be observed in Fig. 7a that the microstructure contains a high number density of plate-shaped precipitates, uniformly dispersed within the α-Mg matrix. The SAED pattern of the $[0001]_\alpha$ zone axis, Fig. 7b, shows extra diffraction spots at 1/2 distance of $\{1\bar{1}00\}_\alpha$or $\{2\bar{1}\bar{1}0\}_\alpha$with the ones surrounding them. Such a diffraction feature is typical in Mg–RE alloys containing a cbco structure phase, namely β', with lattice parameters $a = 2 \times a_{\alpha\text{-Mg}} = 0.64$ nm, $b = 8 \times d(10\bar{1}0)_{\alpha-\text{Mg}} = 2.22$ nm, $c = c_{\alpha\text{-Mg}} = 0.52$ nm, being in agreement with other studies on these alloys [8, 9]. The orientation relationship between the β' phase and the matrix implied by SAED is $[001]_{\beta'}//[0001]_\alpha$, $(100)_{\beta'}//(2\bar{1}\bar{1}0)_\alpha$. The results indicate that the β' plates form on the $\{1\bar{1}00\}_\alpha$ or $\{2\bar{1}\bar{1}0\}_\alpha$ prismatic planes of α-Mg and the

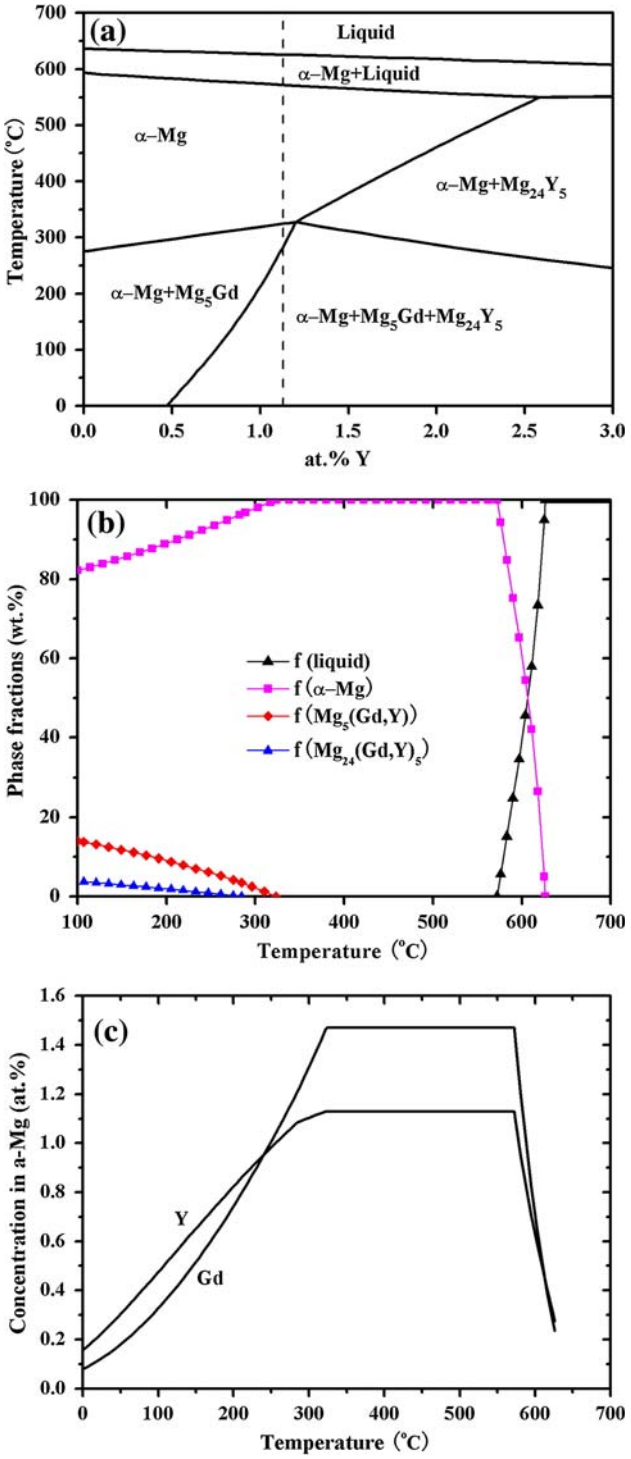

Fig. 5 **a** Calculated equilibrium phase diagram of the Mg–1.48Gd–*x*Y (at.%) alloy system. The *dashed line* corresponds to the alloy in this study (Mg–1.48Gd–1.13Y). **b** Calculated phase fraction (wt%) and **c** Gd and Y concentrations (at.%) in α-Mg at equilibrium as a function of temperature for the investigated alloy

angle between the habit plane of the precipitate plates and $(0001)_\alpha$ slip plane is 90°. The cross-section of the prismatic plates intersected in the slip plane is approximately

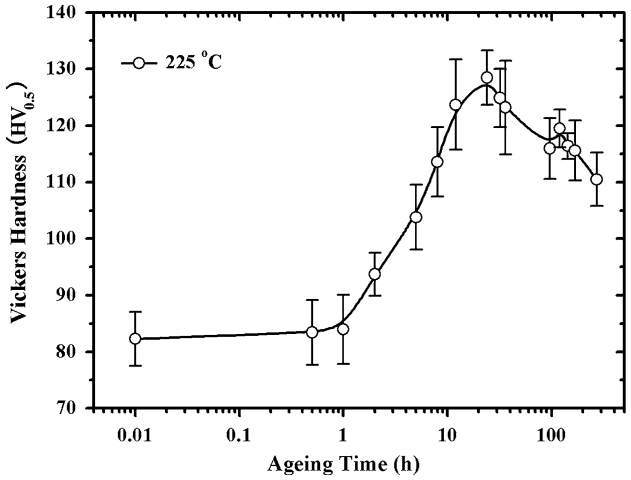

Fig. 6 Ageing hardening response of the solution-treated alloy at 225 °C

rectangular in shape, defined by the mean planar thickness t_p (=15 nm) and the mean planar diameter d_p (=31 nm), as shown in the inset in Fig. 7a [21].

With continued ageing for 168 h, the SAED pattern indicates that the over-aged microstructure still contains predominantly metastable β' precipitates, which grow to $\sim$ 66 nm in diameter and $\sim$ 17 nm in thickness, as shown in Fig. 7c (B//$[0001]_\alpha$).

In addition to the β' precipitates predominantly dispersed within the α-Mg phase matrix, precipitates are also observed along the grain boundaries, as shown in Fig. 8. The SAED pattern corresponding to Figs. 7a and 8 is the same, as shown in Fig. 7b, which indicates that the grain boundary also contains the metastable β' phase.

Tensile mechanical properties

The results from room temperature tensile tests of the as-cast, solution-treated, peak-aged and over-aged alloy are presented in Fig. 9 and Table 3. Table 3 also includes the true yield strength, i.e. accounting for the cross-sectional area reduction. Compared to the as-cast Mg–1.48Gd–1.13Y–0.16Zr alloy, solution treatment results in a great enhancement in elongation accompanied by a relatively small increase in ultimate tensile strength (UTS). However, its tensile yield strength (TYS) decreases. Further ageing leads to a significant enhancement in UTS and TYS. Specifically, the peak-aged alloy exhibits the highest strength and the UTS and TYS are 370 and 277 MPa, respectively. Unfortunately, the peak-aged alloy displays a considerable decrease in ductility; this strengthening effect and loss in ductility are believed to be due to β' precipitation, as will be discussed in the following section. In spite of the limited

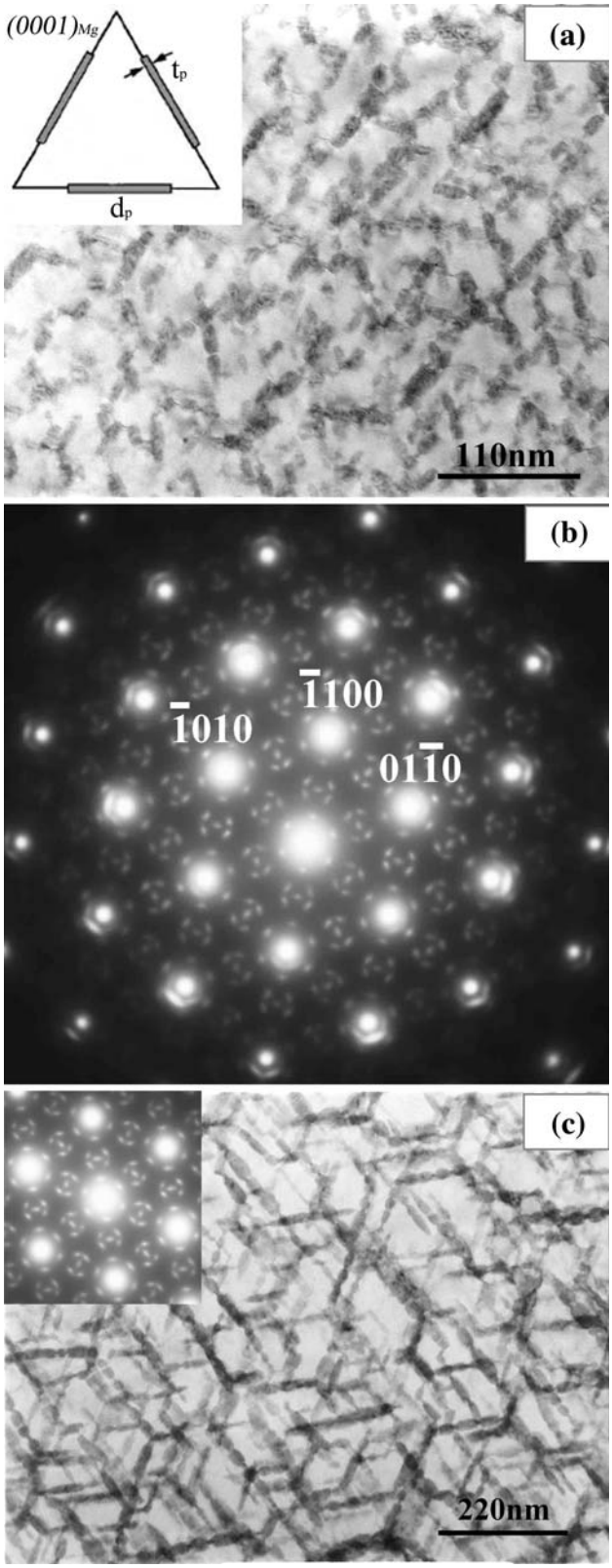

Fig. 7 **a** TEM bright field image taken along the $[0001]_\alpha$ zone axis and **b** the corresponding SAED pattern recorded from a peak-aged (24 h) sample. **c** $[0001]_\alpha$ TEM bright field image recorded from the over-aged sample; inset shows the corresponding SAED pattern

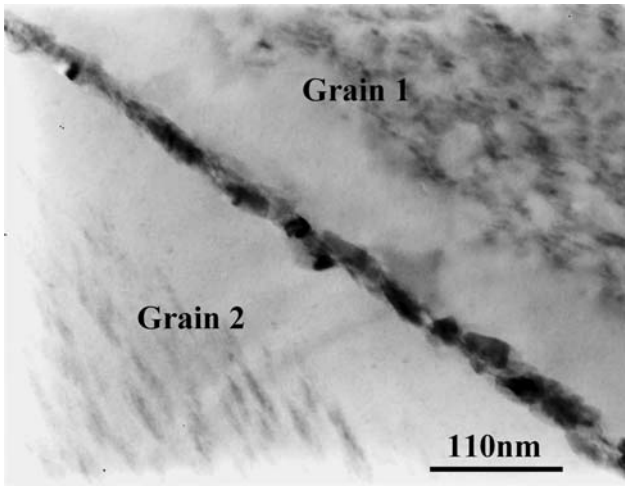

Fig. 8 Grain boundary in the peak-aged Mg–1.48Gd–1.13Y–0.16Zr alloy showing finely distributed precipitate formed during the ageing process

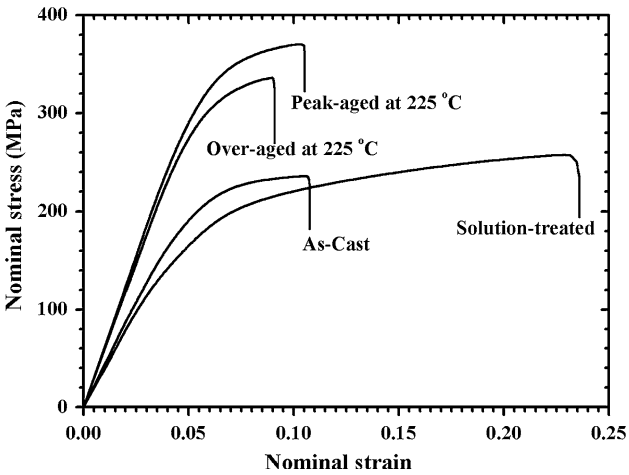

Fig. 9 Typical nominal stress–strain curves at room temperature for the Mg–1.48Gd–1.13Y–0.16Zr alloy in various conditions

ductility, the results indicate that it is possible to obtain a desirable strength enhancement in the Mg–1.48Gd–1.13Y–0.16Zr magnesium alloy after appropriate heat treatment. Moreover, the over-aged sample shows slightly lower strength and elongation than the peak-aged sample.

The effect of temperature on the strength and elongation of the peak-aged Mg–1.48Gd–1.13Y–0.16Zr samples are shown in Fig. 10. It is noted that the alloy shows a high strength of more than 310 MPa and the strength declines slowly from room temperature to 250 °C. This is mainly due to the presence of thermal stable β' precipitates within the matrix and along the grain boundaries. As the temperature further increases to 300 °C, the strength steeply decreases to 184 MPa while the elongation of the alloy remarkably increases to 33%.

Table 3 Tensile properties of the Mg–1.48Gd–1.13Y–0.16Zr alloy at room temperature

Temper	TYS (MPa)		UTS (MPa)	Elongation (%)
	True	Nominal	Nominal	Nominal
As–cast	177	159	231	5.2
Solution-treated	134	126	258	16.6
Peak-aged at 225 °C for 24 h	304	277	370	4.5
Over-aged at 225 °C for 168 h	285	261	336	3.3

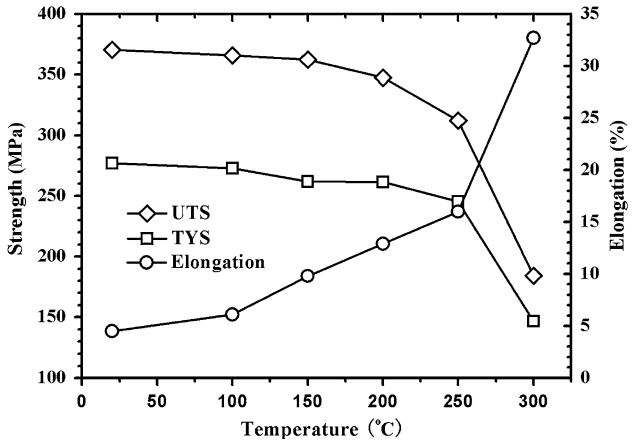

Fig. 10 Average strength and elongation of the peak-aged Mg–1.48Gd–1.13Y–0.16Zr alloy as a function of temperature

Discussion

Strengthening mechanisms

Rare earth elements (RE) are the most effective elements to improve the strength of magnesium alloys. The strengthening mechanisms for alloys in different conditions may typically be divided into (i) strengthening due to eutectics (hereafter denoted as second phase strengthening, σ_{sp}), (ii) solid solution strengthening (σ_{ss}), (iii) grain boundary strengthening (σ_{gb}) and (iv) precipitation strengthening (σ_{ppt}) [5, 7, 16]. A possible expression of the yield strength (σ_{ys}) of an alloy can be approximated as a sum of these contributions: $\sigma_{ys} = \sigma_{gb} + \sigma_{ss} + \sigma_{sp} + \sigma_{ppt}$. The modelled yield strength is expected to give a closer representative value of the true yield strength than the nominal one (Table 3). Combining the data obtained from experiments and thermodynamic calculations, the magnitude of individual contributions can be quantitatively estimated.

Grain boundary strengthening σ_{gb}

The grain size contribution to the yield strength can be evaluated using the well known Hall–Petch relation. A value of 11 MPa from Hauser et al. [22] is used for the intrinsic lattice resistance to basal slip [16], σ_0:

$$\sigma_{gb} = \sigma_0 + kd^{-1/2}, \tag{1}$$

where d is the grain size of the material and k is a parameter that describes the relative strengthening contributions of grain boundaries. A k value of 188 MPa $\mu m^{1/2}$, taken from a previous study [23], was used in this study.

Solid solution strengthening σ_{ss}

The solid solution strengthening term includes the substitutional strengthening from both Gd and Y atoms in the matrix. Preceding studies [23, 24] on Mg–RE single phase alloys have clearly shown that the solid solution strengthening effect due to multiple alloying additions in Mg–Gd–Y ternary alloys can be evaluated as:

$$\Delta\sigma_{ss} = \left(C_{Gd}^{1/n}X_{Gd} + C_{Y}^{1/n}X_{Y}\right)^{n} \tag{2}$$

where $n = 2/3$, X_{Gd} and X_Y are the atomic fraction of solute, C_{Gd} (1168 MPa (at.%) $^{-2/3}$) and C_Y (1249 MPa (at.%) $^{-2/3}$) are the binary alloy strengthening rates. This model has been found suitable to predict the yield strength of solid solution alloys for a series of Mg–Gd–Y alloys [23].

Precipitation strengthening (Orowan mechanism) σ_{ppt}

The microstructural investigation (Figs. 7 and 8) of this alloy indicates that most of the particles in the aged Mg–Gd–Y alloy are the plate-shaped β' phase that forms on the prismatic planes of α-Mg. Nie [21] reported the effect of the shape and orientation of precipitates on Orowan strengthening in Mg alloys. According to his results, the plate-like precipitates which form on the prismatic planes, $\{10\bar{1}0\}_{Mg}$ or $(2\bar{1}\bar{1}0)_{Mg}$, are more effective for Orowan strengthening than spherical particles, plates on the basal planes and rods. If the prismatic plates are assumed to have an ideal arrangement at the centre of each surface of a triangular volume in the matrix phase (inset in Fig. 7a [21]), then the increase in strength due to the prismatic precipitate plates is described as

$$\sigma_{Orowan} = \frac{MGb}{2\pi\sqrt{1-\upsilon}\left(0.931\sqrt{\frac{d_p t_p}{f}} - 0.5d_p - 0.886t_p\right)} \times \ln\frac{\sqrt{d_p t_p}}{b} \tag{3}$$

where M is the Taylor factor, G is the shear modulus of the magnesium matrix phase, **b** is the magnitude of the Burgers vector for basal slip in hcp Mg, υ is the Poisson's ratio, f is the volume fraction of particles, d_p and t_p are, respectively, the mean planar diameter and thickness of precipitates in the slip plane.

Strengthening due to eutectics σ_{sp}

In contrast with precipitation strengthening, the quantitative model on the effect of the eutectic phases was unknown. Therefore, σ_{sp} was determined by subtracting other strengthening contributions from the total yield strength.

Evaluation of strengthening contributions

The values of all the parameters [7, 16, 22–25] involved in the following calculations are presented in Table 4.

The as-cast Mg–1.48Gd–1.13Y–0.16Zr alloy consists mainly of the α-Mg solid solution and eutectic compounds (Fig. 1). Therefore, in as-cast alloy, solid solution strengthening (σ_{ss}), second phase strengthening (σ_{sp}) and grain boundary strengthening (σ_{gb}) contribute to the total strength. The calculated contribution of grain boundary strengthening (σ_{gb}) to the strength is approximately 35 MPa for the as-cast Mg–1.48Gd–1.13Y–0.16Zr alloy with an average grain size of 61 μm. The concentrations of Gd and Y in the as-cast α-Mg matrix are shown in Table 2 and the solid solution strengthening can be estimated to be about 73 MPa according to Eq. 2. A 7% volume fraction of eutectic compounds results in about $\sigma_{sp} = \sigma_{ys} - \sigma_{gb} - \sigma_{ss} = 177 - 35 - 73 = 69$ MPa, where the value of σ_{ys} is measured from tensile tests. The eutectics are complex in shape with large aspect ratios and are prone to fracture at local stress concentrations during tensile test, just like the $Mg_{17}Al_{12}$ compound in Mg–Al alloys [26]. The microcracks form easily by the fracture of eutectic compounds as shown in Fig. 11. Hence, the as-cast alloy has the lowest tensile strength, being about 231 MPa (see Fig. 7 and Table 3).

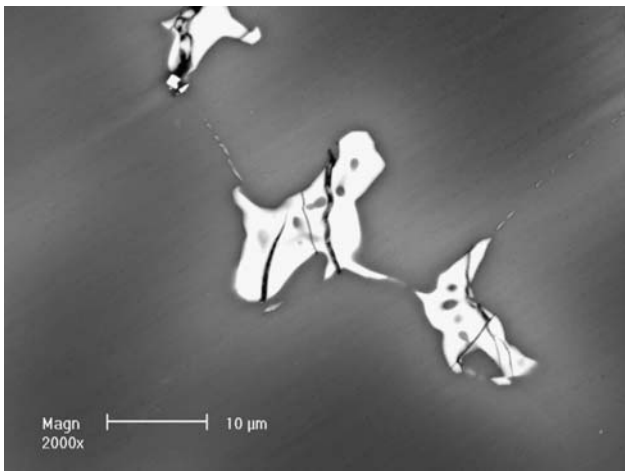

Fig. 11 Longitudinal section of the tensile-tested as-cast Mg–1.48Gd–1.13Y–0.16Zr alloy showing the fragmentation of the eutectic $Mg_{24}(Gd,Y)_5$ phase (stress axis is horizontal)

In the case of the solution-treated alloy, the calculated contribution of grain boundary strengthening to the strength is approximately 29 MPa for the alloy with an average grain size of 108 μm. If all the alloying elements are assumed to dissolve into the matrix, the yield strength of solution-treated alloy in that case can be calculated to be $\sigma_{ys} = \sigma_{gb} + \sigma_{ss} = 29 + 106 = 135$ MPa, which is in good agreement with the experimental value (134 MPa in Table 3).

As can be seen from Figs. 7 and 8, the peak-aged microstructure contains predominantly the metastable β' phase within the matrix and along the grain boundaries. The alloying elements of Gd and Y are portioned between two phases: the magnesium-based solid solution and the precipitates. The concentrations of Gd and Y in the matrix, as well as the fraction of nanoscale precipitates, are not easy to be determined by analytical electron microscopy alone. In this case, the solute concentrations and the fraction of precipitates are estimated according to the

Table 4 Parameters and values used in the thermodynamic calculations

Parameter	Description	Value used	Reference
σ_0	Intrinsic lattice strength in hcp Mg	11 MPa	[16, 22]
k	Hall–Petch parameter	188 MPa $\mu m^{1/2}$	[23]
d	hcp Mg matrix grain size	61, 108 μm	This work
C_{Gd}	Solid solution strengthening rate of Gd in Mg	1168 MPa $(at.\%)^{-2/3}$	[23]
C_Y	Solid solution strengthening rate of Y in Mg	1249 MPa $(at.\%)^{-2/3}$	[24]
M	Taylor factor	3	[25]
G	Shear modulus of hcp matrix	16.6	[7]
b	Burgers vector for basal slip in hcp Mg	0.32 nm	[16, 25]
υ	Poisson's ratio	0.35	[7]

calculated equilibrium phase diagram due to the fact that the aged alloy approaches thermal equilibrium [8]. As seen in Fig. 5c, the concentrations of Gd and Y in the solid solution at 225 °C are about 0.87 and 0.91 at.%, respectively, resulting in $\sigma_{ss} = 82$ MPa. According to the density (g/cm^3) of Mg (1.74) [27], $Mg_{24}(Gd,Y)_5$ (2.39) [28] and $Mg_5(Gd,Y)$ (3.03) [29] and the equilibrium weight fraction of $Mg_{24}(Gd,Y)_5$ (1.35 wt%), $Mg_5(Gd,Y)$ (7.49 wt%) phase at 225 °C (Fig. 5b), the volume fraction of $Mg_{24}(Gd,Y)_5$ and $Mg_5(Gd,Y)$ are 1.01 and 4.44 vol.%, respectively. Given that the residual cuboid-shaped $Mg_5(Gd,Y)$ phase is about 1 vol.% (Fig. 4), the volume fraction of the precipitates is assumed to be 4.45 vol.%. Therefore, the precipitation strengthening contribution is calculated to be 200 MPa according to Eq. 3. The same procedure has been applied to the over-aged sample and $\sigma_{ppt} = 156$ MPa has been obtained.

The magnitudes of the individual strengthening contributions for the Mg–1.48Gd–1.13Y–0.16Zr alloy in various conditions are summarized in Table 5. As can be seen, in the peak-aged condition, the maximum strengthening due to the Orowan mechanism of precipitates is ~200 MPa. The modelled yield strength is calculated by linearly summing the contributions described in "Grain boundary strengthening σ_{sp}" through "Strengthening due to eutectics σ_{sp}" and is compared with the experimental values in Table 5. Good agreement, with an error of 0.7–6.3%, has been obtained.

Strengthening due to β' precipitates

One of the outstanding features of the Mg–1.48Gd–1.13Y–0.16Zr alloy is the possibility to show a substantial strengthening effect during the decomposition of the supersaturated magnesium solid solution (see Fig. 5b). The superior strength and thermal stability until 250 °C obtained in the peak-aged Mg–1.48Gd–1.13Y–0.16Zr alloy are attributed to the thermally stable precipitate β' phase (Figs. 7 and 8) which is a metastable version of the β phase (similar composition, Mg_5RE [8]). The plate-shaped β' precipitates, which form on the prismatic planes of the magnesium matrix, are vertical to the basal plane of α-Mg, providing the most effective obstacles to basal dislocation slip [21]. The better thermal stability of the β' phase in Mg–Gd–Y–Zr alloys was also suggested to be responsible for the superior creep resistance to WE54 [9, 10, 30].

TEM analysis reveals that the β' phase is likely to maintain its crystal structure and morphology from the peak-aged through the over-aged conditions. Equation 3 describes the increase in strength due to the prismatic precipitates as observed in the aged alloy. In the present case, f, G, υ, $\mathbf{b}$ remain constant, while the diameter of the precipitates has been increased from 31 nm in the peak-aged condition to 66 nm in the over-aged alloy. Thus, the decrease in the hardness (Fig. 6) and strength (Fig. 9) can be attributed to the coarsening of the particles and the decreased number density of precipitates in the over-aged alloy compared to the peak-aged alloy.

Increasing temperature to 300 °C leads to a rapid decrease in strength (Fig. 10). This is considered to be the result of the recovery effect of the aged Mg–Gd–Y alloy during exposure at a higher temperature. A typical $[0001]_\alpha$ TEM micrograph of the specimens after tensile testing at 300 °C is shown in Fig. 12. It is obvious that some of the precipitates have disappeared, and as a result, the volume fraction significantly decreases. This is consistent with the results of Rokhlin and Nikitina [31], who observed that a significant recovery effect after ageing in Mg–12wt.%Y and Mg–24wt.%Gd alloys took place as a result of the precipitate instability at a higher temperature. This process can be easily understood according to the equilibrium phase diagram. For the Mg–1.48Gd–1.13Y–0.16Zr alloy, the calculated solubility limit of Gd in α-Mg increases from ~0.87 at.% at 225 °C to 1.31 at.% at 300 °C, while the solubility limit of Y increases from 0.91 at.% at 225 °C to 1.10 at.% at 300 °C (Fig. 5c). The relatively larger solubilities at 300 °C result in the partial dissolution of the precipitates.

Furthermore, the prismatic precipitate plates are thought to be less effective obstacles to dislocations gliding on the non-basal plane or cross slip activated at an elevated temperature, because they are not perpendicular to the slip planes any more so that the effective area as obstacle to

Table 5 Individual strengthening contributions (MPa) in the Mg–1.48Gd–1.13Y–0.16Zr alloy at room temperature

Alloy condition	As-cast	Solution-treated	Peak-aged	Over-aged
Solid solution strengthening, σ_{ss}	73	106	82	82
Grain boundary strengthening, σ_{gb}	35	29	29	29
Second phase strengthening, σ_{sp}	69	0	0	0
Precipitation strengthening, σ_{ppt}	0	0	200	156
Calculated yield strength, σ_{ys}	–	135	311	267
Experimental yield strength, σ_{ys}	177	134	304	285
Error (%)	–	+0.7	+2.3	−6.3

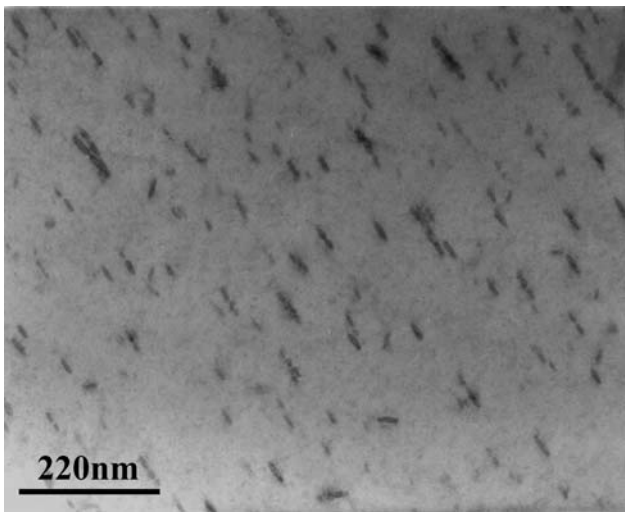

Fig. 12 $[0001]_{\alpha}$ TEM bright image of the peak-aged sample after tensile testing at 300 °C

dislocation slip decreases [5]. It is probably another reason why the strength of the alloy steeply decreases at temperatures above 250 °C.

Application of the thermodynamic calculations

The thermodynamic assessment of the Mg–Gd–Y system contributes to a better understanding of the above strengthening mechanisms in the investigated alloy and to the development of new heat treatable alloys. The aim of this discussion is to emphasize the applicability of thermodynamic calculations in predicting the alloy microstructure during a heat treatment process and the impact of the treatment on the alloy properties.

The alloy composition was chosen as Mg–1.48Gd–1.13Y–0.16Zr (at.%), having in view the purpose of this study, namely the abilities: (i) to undergo a rapid and thorough dissolution of the solute atoms during a solution treatment and (ii) to precipitate a large number of RE-based precipitates during an ageing treatment. The solution treatment at 525 °C that will lead to a single-phase material is generally selected according to the equilibrium phase diagram.

Some quite satisfactory results have been obtained from the thermodynamic calculations for the Mg–Gd–Y alloy. The phases presented in the as-cast structure of the studied alloy are in good agreement with those expected by the thermodynamic calculation. The calculation predicted no RE-containing compound in the microstructure of the solution-treated alloy where a single phase material can be obtained. Indeed, this correlates well with the dissolution of the $Mg_{24}(Gd,Y)_5$ phase. However, as shown above, the cuboid-shaped phase with a higher RE content (Table 2) was detected in the alloy studied. This is probably because the diffusivity of RE in Mg is significantly low [32], which is not taken into account in the calculation. Indeed, the crystal structure of the cuboid-shaped phase and its exact phase composition range are still under dispute [5, 33]. Further work is needed to clarify this discrepancy.

Conclusions

The phase constituent and microstructure evolution of a Mg–1.48Gd–1.13Y–0.16Zr (at.%) alloy during solidification, solution treating and age hardening are predicted qualitatively and quantitatively based on computational thermodynamics. This includes choosing the alloy composition and various heat-treatment routes, which is aimed at obtaining a significant improvement in the alloy strength. The thermodynamic predictions are confirmed experimentally through detailed microstructure investigations.

The heat-treatment routes selected by thermodynamic calculation result in a significant improvement in the alloy hardness and strength. The typical ultimate tensile strength, tensile yield strength and elongation of the peak-aged alloy are 370, 277 MPa and 4.5%, respectively. The high strength at temperatures lower than 250 °C is mainly attributed to the high number density of the plate-shaped β' precipitates within the matrix and along the grain boundaries. A significant decrease in strength at 300 °C is mainly attributed to the recovery effect which leads to a significant dissolution of the β' precipitates. For ageing treatments up to 168 h at 225 °C, the microstructure shows the coarsening of the plated-shaped β' precipitates and a decrease in the number density of the precipitates, resulting in a slight decrease in the hardness and strength of the over-aged sample.

The strength of the alloy in different conditions is determined by a combination of grain boundary strengthening, solid solution strengthening due to Gd and Y atoms and precipitation strengthening due to the β' phase and strengthening by the eutectic compounds. According to both the thermodynamic predictions and the experimental measurements, the individual strengthening contributions are quantified. The modelled yield strength is compared with experimental results and a reasonable agreement is reached.

Acknowledgements The authors gratefully acknowledge the financial support from the National Basic Research Program of China (973 Program) through project no. 2007CB613704. Assistance of Dr. W. Tang with TEM analysis is also gratefully acknowledged.

References

1. Park JP, Kim MG, Yoon US, Kim WJ (2009) J Mater Sci 44:47. doi:10.1007/s10853-008-3130-z

2. Figueiredo RB, Langdon TG (2008) J Mater Sci 43:7366. doi:10.1007/s10853-008-2846-0
3. Liu Y, Yuan GY, Lu C, Ding WJ, Jiang JZ (2008) J Mater Sci 43:5527. doi:10.1007/s10853-008-2839-z
4. Wang J, Meng J, Zhang D, Tang D (2007) Mater Sci Eng A 456:78
5. He SM, Zeng XQ, Peng LM, Gao X, Nie JF, Ding WJ (2007) J Alloys Compd 427:316
6. Gao X, He SM, Zeng XQ, Peng LM, Ding WJ, Nie JF (2006) Mater Sci Eng A 431:322
7. Yang Z, Li JP, Guo YC, Liu T, Xia F, Zeng ZW, Liang MX (2007) Mater Sci Eng A 454–455:274
8. Honma T, Ohkubo T, Hono K, Kamado S (2005) Mater Sci Eng A 395:301
9. He SM, Zeng XQ, Peng LM, Gao X, Nie JF, Ding WJ (2006) J Alloys Compd 421:309
10. Anyanwu IA, Kamado S, Kojima Y (2001) Mater Trans 42:1212
11. Smola B, Stulıkova I, Buch Fv, Mordike BL (2002) Mater Sci Eng A 324:113
12. Peng QM, Wu YM, Fang DQ, Meng J, Wang LM (2007) J Mater Sci 42:3908. doi:10.1007/s10853-006-0451-7
13. Wu YJ, Lin DL, Zeng XQ, Peng LM, Ding WJ (2009) J Mater Sci 44:1607. doi:10.1007/s10853-008-3213-x
14. Lin L, Chen LJ, Liu Z (2008) J Mater Sci 43:4493. doi:10.1007/s10853-008-2650-x
15. Nie JF, Oh-ishi K, Gao X, Hono K (2008) Acta Mater 56:6061
16. Hutchinson CR, Nie JF, Gorrse S (2005) Metall Mater Trans 36A:2093
17. Li X, Miodownik AP, Saunders N (2001) J Phase Equilib 22:247
18. Guo CP, Du ZM, Li CR (2007) CALPHAD 31:75
19. Guo YC, Li JP, Li JS, Yang Z, Zhao J, Xia F, Liang MX (2008) J Alloys Compd 450:446
20. Dinsdale AT (1991) CALPHAD 15:317
21. Nie JF (2003) Scr Mater 48:1009
22. Hauser FE, Landon PR, Dorn JE (1956) AIME Trans 206:589
23. Gao L, Chen RS, Han EH (2009) J Alloys Compd 481:379
24. Gao L, Chen RS, Han EH (2009) J Alloys Compd 472:234
25. Suzuki M, Sato H, Maruyama K, Oikawa H (1998) Mater Sci Eng A 252:248
26. Dahle AK, Lee YC, Nave MD, Schaffer PL, StJohn DH (2001) J Light Met 1:61
27. Friedrich HE, Mordike BL (2006) Mg technology. Springer, Berlin, Heidelberg
28. Zhang MX, Kelly PM (2005) Acta Mater 53:1085
29. Fornasini ML, Manfrinetti P (1986) Acta Crystallogr C42:138
30. Liu K, Zhang JH, Sun W, Qiu X, Lu HY, Tang DX, Rokhlin LL, Elkin FM, Meng J (2009) J Mater Sci 44:74. doi:10.1007/s10853-008-3122-z
31. Rokhlin LL, Nikitina NI (1998) J Alloys Compd 279:166
32. Zhu SM, Nie JF (2004) Scr Mater 50:51
33. Gao Y, Wang Q, Gu J, Zhao Y, Tong Y (2007) Mater Sci Eng A 459:117